Contrib Mineral Petrol (2015) 169:37
DOI 10.1007/s00410-015-1132-9

ORIGINAL PAPER

Melting of metasomatized peridotite at 4–6 GPa and up to 1200 °C: an experimental approach

R. Kessel[1] · **T. Pettke**[2] · **P. Fumagalli**[3]

Received: 20 March 2014 / Accepted: 20 March 2015 / Published online: 3 April 2015

Abstract The phase assemblages and compositions in a K-bearing lherzolite + H_2O system are determined between 4 and 6 GPa and 850–1200 °C, and the melting reactions occurring at subarc depth in subduction zones are constrained. Experiments were performed on a rocking multi-anvil apparatus. The experiments had around 16 wt% water content, and hydrous melt or aqueous fluid was segregated and trapped in a diamond aggregate layer. The compositions of the aqueous fluid and hydrous melt phases were measured using the cryogenic LA-ICP-MS technique. The residual lherzolite consists of olivine, orthopyroxene, clinopyroxene, and garnet, while diamond (C) is assumed to be inert. Hydrous and alkali-rich minerals were absent from the run products due to preferred dissolution of K_2O (and Na_2O) to the aqueous fluid/hydrous melt phases. The role of phlogopite in melting relations is, thus, controlled by the water content in the system: at the water content of around 16 wt% used here, phlogopite is unstable and thus does not participate in melting reactions. The water-saturated solidus, i.e., the first appearance of hydrous melt in the K–lherzolite composition, is located between 900 and 1000 °C at 4 GPa and between 1000 and 1100 °C at 5 and 6 GPa. Compositional jumps between hydrous melt and aqueous fluid at the solidus include a significant increase in the total dissolved solids load. All melts/fluids are peralkaline and calcium-rich. The melting reactions at the solidus are peritectic, as olivine, clinopyroxene, garnet, and H_2O are consumed to generate hydrous melt plus orthopyroxene. Our fluid/melt compositional data demonstrate that the water-saturated hybrid peridotite solidus lies above 1000 °C at depths greater than 150 km and that the second critical endpoint is not reached at 6 GPa for a K_2O–Na_2O–CaO–FeO–MgO–Al_2O_3–SiO_2–H_2O–Cr_2O_3(–TiO_2) peridotite composition.

Keywords High-pressure experiments · Aqueous fluids · Hybrid mantle · Metasomatized peridotite · Hydrous melts · Subduction zone · Water-saturated solidus

Introduction

The Earth's upper mantle is mainly composed of peridotite. Hydration of the mantle peridotite, due to the introduction of water-rich fluids from the subducting lithosphere, is one of the main processes leading to metasomatism and partial melting, the processes governing Earth evolution. Water-bearing magmas are the medium by which mass transfer occurs between major reservoirs in the Earth interior. These material fluxes control the distribution of elements in the Earth and therefore cooling of the Earth and occurrence of ore deposits of economic importance. Metasomatism of the mantle by alkali-rich fluids from the slab is also evident by the sporadic occurrence of phlogopite-bearing peridotitic xenoliths (e.g., Nixon 1987) and of phlogopite-bearing

---

Communicated by Jon Blundy and Othmar Müntener.

Electronic supplementary material The online version of this article (doi:10.1007/s00410-015-1132-9) contains supplementary material, which is available to authorized users.

✉ R. Kessel
ronit.kessel@mail.huji.ac.il

[1] Institute of Earth Science, The Hebrew University of Jerusalem, Givat-Ram, 91904 Jerusalem, Israel

[2] Institute of Geological Sciences, University of Bern, 3012 Bern, Switzerland

[3] Dipartimento di Scienze della Terra, Università degli Studi di Milano, Milan, Italy

peridotites in orogenic ultra-high-pressure terrains (e.g., Rampone and Morten 2001). Peridotite enriched in potassic phases is included within 'metasomatized mantle' or 'hybrid mantle.' Such peridotites occur within the mantle wedge and can be subject to melting to eventually form continental crust.

The amount of water structurally bound in mantle minerals is controlled by the stability fields of hydrous phases as well as nominally anhydrous minerals. At depths below some 150 km, several hydrous minerals can be stable, such as antigorite, chlorite, 10Å phase, phlogopite, while talc and amphibole are stable at smaller depth (e.g., Pawley and Wood 1995; Fumagalli et al. 2001, 2009; Dvir et al. 2011). The main hydrous phases stable in K-bearing peridotites at some 150 km, beyond the stability field of pargasitic amphibole, are 10 Å phase, K-richterite, and phlogopite (Konzett and Ulmer 1999; Fumagalli et al. 2009). With increasing pressure, the water storage capacity in mineral structures tends to decrease substantially, to several hundreds of µg/g only, bound in nominally anhydrous minerals (e.g., olivine, pyroxene, garnet) at higher temperatures or in rare hydrous phases (e.g., dense hydrous magnesium silicates) at lower temperatures. Any 'excess' water in the mantle leads to the formation of an aqueous fluid phase below, or a hydrous melt above the 'water-saturated solidus,' or a supercritical fluid beyond the second critical endpoint (e.g., Melekhova et al. 2007). Understanding the temperature of hydrous melting (the location of the water-saturated solidus) of various mantle materials in general, and of metasomatized peridotites in particular, and the properties of these fluids and melts is a fundamental constraint for geodynamic modeling.

The role of H_2O in melting of the various mantle peridotite compositions has been investigated intensely over the past 50 years. The location of the water-saturated solidus for phlogopite-absent peridotite is still strongly debated (e.g., Kushiro et al. 1968; Millhollen et al. 1974; Mysen and Boettcher 1975; Grove et al. 2006; Mibe et al. 2007; Green et al. 2010; Till et al. 2012a; Spandler et al. 2014; Green et al. 2014). Proposed temperatures for the water-saturated solidus differ by 200–400 °C over the pressure range of 2.5–5 GPa (Fig. 1). Melting of metasomatized phlogopite-bearing peridotite and the role alkali elements play in resulting magmas are only sparsely investigated (e.g., Green 1973; Mengel and Green 1989; Thibault and Edgar 1992; Conceição and Green 2004; Green et al. 2014) and also reveal disagreement with respect to the solidus location (Fig. 1). In addition, the composition of these H_2O-bearing mantle melts is still poorly quantified.

Here, we focus on the water-saturated melting of a metasomatized peridotite and present a new experimental dataset on the major element systematics of all phases in a K-rich lherzolite–H_2O system at 4–6 GPa and 850–1200 °C. We use recently developed experimental and analytical methods allowing for the direct measurement of the composition of all phases, solids as well as liquids, in each experiment. Diamond-trap experiments are performed in a rocking multi-anvil press in order to enhance reaction rates and equilibration, thus preventing the formation of chemically zoned capsules (Schmidt and Ulmer 2004). After the termination of the experiment, the fluid/melt phase is analyzed using the cryogenic laser ablation (LA-)ICP-MS technique (Kessel et al. 2004). The minerals are analyzed using electron probe microanalysis (EPMA). The combination of these experimental and analytical techniques allows us to define the location of the water-saturated peridotite solidus at 120–180 km depth (4–6 GPa) and to study the reactions occurring among the phases across the water-saturated solidus. In contrast to procedures commonly adopted in the past, we rely on melt/fluid phase compositions instead of the solid mineral compositions and/or textural criteria to define the location of the water-saturated solidus of the system, thereby avoiding ambiguity resulting from the textural similarity of quench phases formed from aqueous fluids and those formed from hydrous melts equilibrated at near-solidus temperatures.

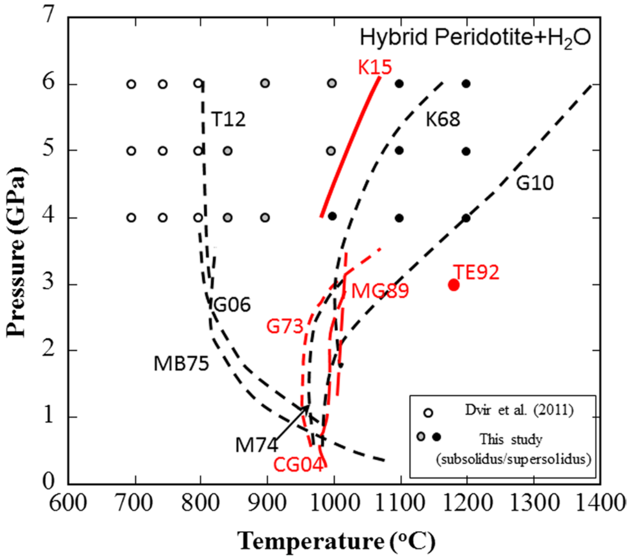

Fig. 1 Literature compilation of solidi in the K-poor (in *black*) and K-rich (in *red*) lherzolite + H_2O systems. K68 = Kushiro et al. (1968); G73 = Green (1973); M74 = Millhollen et al. (1974); MB75 = Mysen and Boettcher (1975); MG89 =Mengel and Green (1989); TE92 = Thibault and Edgar (1992); CG04 = Conceição and Green (2004); G06 = Grove et al. (2006); G10 = Green et al. (2010, 2014); T12 = Till et al. (2012a). Superimposed on the compilation are the P–T conditions of experiments performed by Dvir et al. (2011) and in this study. The resultant water-saturated solidus in this study is given as a *black thick line* labeled K15

Experimental procedure and analytical techniques

Starting materials

The current study focuses on the K_2O–Na_2O–CaO–FeO–MgO–Al_2O_3–SiO_2–H_2O–Cr_2O_3(–TiO_2) (KNCFMASH) system. The peridotitic starting material used in this study is a synthetic K-bearing lherzolite (KLZ) similar to that used by Konzett and Ulmer (1999) and Fumagalli et al. (2009). A similar bulk composition, lacking Cr_2O_3, TiO_2, and K_2O, was used in Dvir et al. (2011) at lower temperatures. This peridotite composition is based on the M. Briançon spinel lherzolite (French Central Massif) with an additional 5 wt% phlogopite and 0.4 wt% Na_2O and final subtraction of 30 wt% of olivine (Fo_{91}) to enhance the abundance of minor phases (i.e., phlogopite and pyroxenes). It was prepared as a gel using tetraethyl orthosilicate (TEOS) as silica source, pure Na-, Ca-, K-, Mg-, and Al-nitric solutions, and ferric benzoate, following the method of Hamilton and Henderson (1968). The gel was fired in a gas-mixing furnace at fO_2 conditions approaching FMQ buffer at 1 atm.

In few of the experiments, the lherzolite starting material was doped with 22 trace elements, ~150 μg/g each (summed to 0.3 wt% of the total bulk composition). The trace element-doped lherzolite is labeled 'KLZT.' The trace element results will be presented elsewhere. The powder was ground in an agate mortar for a total of 4 h and was dried at 110 °C for 10 h. The major element composition of the starting material was determined by dissolving three aliquots in HF–HNO_3 and analyzing these using ICP-MS at the Geological Survey of Israel. The measured composition of the starting material is given in Table 1, compared to LzCs(1) and LzCs(2), the two compositions used in the study of Dvir et al. (2011).

Table 1 Composition of K-rich lherzolite starting material used in this study

Wt%	KLZ this study[b]	LzCs(1)[c]	LzCs(2)[c]
SiO_2	48.13(71)	46.78	49.00
TiO_2	0.084(002)		
Al_2O_3	4.50(05)	3.35	3.38
Cr_2O_3	0.66(01)		
FeO[a]	6.26(130)	6.17	5.55
MgO	36.16(17)	40.40	38.74
CaO	3.46(02)	3.03	3.11
Na_2O	0.86(12)	0.27	0.22
K_2O	0.64(03)		
Total	100	100	100

[a] All Fe is expressed as FeO

[b] The average and 1 SD of the starting material as measured in three aliquots. Numbers enclosed in parentheses indicate 1 standard deviation of the last digits quoted, i.e., 48.13(71) should be read as 48.13 ± 0.71

[c] LzCs(1) and LzCs(2) refer to the major element compositions of the two starting materials used in Dvir et al. (2011)

The experimental setup was similar to that used by Kessel et al. (2004, 2005a, b) and Dvir et al. (2011) and is given in Table 2. The experiments were performed using Au capsules (2.0 mm inner diameter, 2.3 mm outer diameter). Au was chosen as the capsule material as it minimizes Fe loss in hydrous melting experiments although it cannot prevent Fe loss completely at high pressure and temperature (e.g., Gaetani and Grove 1998; Kägi et al. 2005 and others). A few randomly chosen charges were checked for Fe in the Au capsules; however, no Fe loss to the capsule was observed. The loss of Fe into the Au capsule during the experiment was also evaluated from the mass balance calculations performed in order to determine phase abundances (as explained below). The residuals for the anhydrous mass balance calculations are given in Table S1 in the supplement. The Fe residual from the least square calculations was found to be in most cases as low as for other elements. However, in the high-temperature experiments (at 4 GPa: 1100, 1200 °C; 5 GPa: 1100 °C; 6 GPa: 1200 °C) larger residuals were found, suggesting some Fe loss into the capsule material.

First, 1.9–2.7 μl H_2O was added to the capsule (measured with a micropipette and confirmed by weight). The capsule was then filled with 4.7–8.1 mg lherzolitic powder, followed by a thin layer of synthetic diamond grains 15–25 μm in size (2.1–5.4 mg, corresponding to 14–33 wt% of the powder + water + diamond system), and another layer of powder. The total weight of the lherzolite powder was 10.7–19.2 mg. The water concentrations in the experiments correspond to 8–20 wt% of the lherzolite + water system. The amount of water loaded into the capsule is more than needed to fill all the space in between the diamonds, which is made on purpose to minimize the danger for 'sucking peridotite powder material' into the trap. No mineral seeds were added to the starting material, and garnet nucleated in all our runs (see below). The capsule was welded while it was frozen (using liquid nitrogen), and then weighed again to ensure that no loss of material occurred upon welding. The sealed capsule was squeezed into a final cylindrical shape of 2.4–3.7 mm in length, ready for experiment.

Experimental conditions

Experiments were conducted in a 675-ton rocking multi-anvil press at the Institute of Earth Sciences, the Hebrew University of Jerusalem, Israel. Temperature was measured using a Pt–Pt_{10}Rh (type S) thermocouple; reported temperatures are not corrected for the effect of pressure on the

Table 2 Experimental conditions

Exp. #	Bulk comp.[a]	*P* (GPa)	Temp. (°C)[b]	*T* (h)	Temp. range (°C)[c]	H_2O (wt%)[d]	Diamonds (wt%)[e]
OC18	KLZ	4	850	163	17	14	17
OC24	KLZ	4	900	144	18	15	33
RK307	KLZT	4	1000	70.5	18	17	19
RK304	KLZT	4	1100	25	38	14	23
RK309	KLZT	4	1200	2.5	28	14	15
OC26	KLZ	5	850	214	18	16	22
NV9	KLZT	5	1000	41.5	33	17	28
RK306	KLZT	5	1100	24	22	17	15
RK311	KLZT	5	1200	5	25	20	14
OC23	KLZ	6	900	124	26	8	14
RK301	KLZT	6	1000	68	28	15	20
RK300	KLZT	6	1100	20	21	16	24
RK308	KLZT	6	1200	4	28	16	14

[a] *KLZ* K–lherzolite composition, *KLZT* trace element-doped K–lherzolite composition

[b] Temperatures are thermocouple readings, placed at the bottom of the capsule

[c] Temperature range along the capsule is calculated assuming a thermal gradient of 11°/mm (following Konzett et al. 1997)

[d] H_2O (wt%)—weight fraction in % of H_2O in the system powder + H_2O

[e] Diamond (wt%)—weight fraction in % of diamond powder in the system powder + H_2O + diamond

thermocouple EMF. During the runs, temperature was kept constant to within ±2 °C. High-pressure calibration was performed as reported in Dvir et al. (2011).

Experiments were conducted at 4–6 GPa and 850–1200 °C for 2.5–163 h (Table 2). In each experiment, the capsule was placed inside a 19/11 MgO octahedron surrounded by a boron nitride cylinder and a stepped graphite furnace. The capsule was placed in the center of the furnace, and the thermocouple was inserted through the octahedron gaskets and furnace in direct contact with the capsule. Oxygen fugacity was not controlled during our experiments. However, it is estimated to remain close to the QFM buffer at atmospheric pressure as imposed during the preparation of the starting material.

In all experiments, the multi-anvil apparatus was constantly rocked 180° from the beginning of heating until half an hour had elapsed at run conditions to ensure homogeneous and equilibrated crystal nucleation centers. Then, rocking was set to take place every 15 min for the rest of the experiment to enhance reaction rates while maintaining equilibration between the liquid and the solid phases (Schmidt and Ulmer 2004). The experiments were terminated by turning off the furnace power, followed by unloading pressure over 10–15 h. Once unloaded, the length of all assembly parts was measured carefully to determine the exact location of the capsule and the temperature range experienced by it during the experiment. The temperature range over the capsule length was calculated to be between 17 and 38 °C (Table 2), employing a thermal gradient of 11°/mm along the stepped graphite furnace (Konzett et al. 1997). Care was taken to place the diamond layer close to the thermal hot spot of the assembly.

Analytical techniques

The solute composition of the fluid/melt phase was directly measured in each experiment employing the cryogenic LA-ICP-MS technique (Kessel et al. 2004). The intact capsule was longitudinally mounted onto a freezing device of the LA-ICP-MS. When frozen, the capsule was cut open with a razor blade to expose a longitudinal section of the capsule and was kept frozen during LA-ICP-MS analysis. Integrated signal sections were as long as 30 s and avoided the first few seconds in order to avoid signal spikes resulting from particles reaching the ICP. The laser beam size (60–90 μm diameter) was adjusted according to the shape of the diamond layer to be the largest possible, in order to allow for bulk analyses of the trap while avoiding admixture of the surrounding peridotite minerals. This approach prevents uncontrolled, fractionated loss of matter still dissolved in the fluid upon capsule piercing, e.g., KOH (Stalder et al. 2002). No correction for the presence of synthetic diamonds was applied since these do not contain any of the elements of interest in significant quantities. The only trace impurities found in the diamonds used in this study are Ni and Cu.

The diamond traps in RK's experiments were analyzed using a 193-nm ArF New Wave excimer laser system coupled to an Agilent (7500 CX) ORS quadruple mass spectrometer at the Institute of Earth Sciences, the Hebrew

University of Jerusalem, Israel. Diamond traps in experiments OC's and NV9 were analyzed using a 193-nm ArF GeoLas Pro excimer laser system coupled to an ELAN DRC-e quadrupole mass spectrometer at the Institute of Geological Sciences, University of Bern, Switzerland. Similar procedures were employed at these analytical facilities. Details on the instrumental setup, optimization strategies, and operating conditions are reported elsewhere (Pettke et al. 2012). At the Hebrew University of Jerusalem, we analyzed for ^{29}Si, ^{47}Ti, ^{27}Al, ^{53}Cr, ^{57}Fe, ^{24}Mg, ^{43}Ca, ^{23}Na, ^{39}K, and ^{232}Th. The same isotopes were analyzed at the University of Bern, except for ^{49}Ti and ^{25}Mg. Data reduction was done using SILLS (Guillong et al. 2008). Element concentration ratios of the fluid/melt phase were obtained from the LA-ICP-MS analysis by external standardization on SRM-610 from NIST [using preferred element concentrations reported in Spandler et al. (2014) and Jochum et al. (2011)], and internal standardization employed the Th concentrations present in the fluid/melt phase at run pressure and temperature (see below).

Potential pitfalls for such experimental procedure include: (1) Crystal growth in the diamond layer due to dissolution/re-precipitation of crystals (Keppler and Audétat 2005; Green et al. 2010). Including such crystals in the LA-ICP-MS analyses of the diamond trap yields an erroneous composition for the fluid or melt phase as well as the potential of missing phases in the residual mineral assemblage. (2) Under oxidizing conditions, diamonds may interact with the water (e.g., Stalder et al. 2002). Reaction of the trap diamonds with water implies that CO_2 may be present in the fluid/melt phase.

We believe that these potential problems can be avoided or their effect be minimized. (1) As discussed in Aerts et al. (2010), placing the diamond layer at the hot spot of the experimental assembly prevents unwanted equilibrium crystal growth within the diamonds. Both Aerts et al. (2010) as well as Stalder et al. (2002) demonstrated that only quench (i.e., secondary) crystals reside in between the diamond grains. Further discussion of the possible occurrence of this phenomenon in our study is given below. (2) Under oxidizing conditions, diamonds should exhibit specific features associated with their corrosion due to interaction with water-bearing solutions (Fedortchouk et al. 2007, 2010). Careful examination of the post-experiment diamonds could not identify such features. Stalder et al. (2000, 2002) have shown that CO_2 may be present in the fluid or melt phase in similar experiments but only in small amounts ($X\ CO_2 \ll 0.1$). We, therefore, assume that the diamonds in our study remain intact during the experiments. Nevertheless, with the experimental setup used in our study, we cannot preclude the possible presence of minimal carbon dissolution into the fluid or melt phase.

After LA-ICP-MS analysis of the fluid/melt phase in the diamond trap, the capsules were mounted in epoxy and cut through the diamond layer using a diamond saw; the two surfaces in contact with the diamond trap were mounted again in epoxy and polished to expose the solid assembly. Several epoxy impregnations were performed in order to achieve a polished surface. Phase identification and textural relations were examined using EPMA (JEOL 8600) at the Institute of Earth Sciences and an environmental scanning electron microscope (Quanta 200) in the Nano-characterization Center both at the Hebrew University of Jerusalem, Israel. The solid phases were analyzed with an accelerating voltage of 15 keV and a beam current of 10 nA using EDS. Counts were collected for 100 s. All phases were quantified for Si, Al, Cr, Mg, Fe, Ca, Na, and K using silicate and oxide standards. Titanium was not analyzed in the minerals.

Data reduction

Cation concentration ratios of the quenched material from the fluid phase trapped in between the diamond aggregates are obtained from the LA-ICP-MS analysis by external standardization. To convert the cation ratios into absolute masses of elements and determine the water-free liquid composition, the Th added to the starting material was used as an internal standard. Potassium, a highly incompatible element as well, was not used as the internal standard, because we aimed at quantifying its concentration in the fluid or melt by direct measurement. Data for the partition coefficient of Th (K_d^{Th}) between peridotitic minerals and a water-bearing fluid/melt phase are limited in the literature. Ayers (1998) provides partitioning values for Th between peridotite and hydrous melt at 2 GPa and 900–1000 °C, with K_d^{Th} of olivine-melt and orthopyroxene-melt of 0.007, K_d^{Th} of clinopyroxene-melt of 2.0, and K_d^{Th} of garnet-melt of 0.05. The partition coefficients of Th between eclogitic minerals and a liquid phase (fluid or melt) were also evaluated in several studies at various pressures, temperatures, and compositions (e.g., Kessel et al. 2005a; Klimm et al. 2008). Kessel et al. (2005a) and unpublished data directly determined partition coefficients of trace elements including Th between K-free eclogitic minerals and a water-bearing liquid phase at 4–6 GPa and 700–1200 °C, 6 GPa; below and above the second critical endpoint of the basalt–water system. Partition coefficients of Th between garnet and fluid/melt and between clinopyroxene and fluid/melt at 4 GPa were 0.002–0.2 and 0.2, respectively. The fraction of clinopyroxene in our run products is less than 0.1 (Table 4). When using the data of Ayers (1998), the resulting melt/residual peridotite distribution coefficient for Th is of the order of 0.2. When using the data of Kessel et al. (2005a), a K_d^{Th} of the order of 0.02 is obtained. These results vary considerably; however, they confirm that thorium can be taken as incompatible in mantle minerals and thus resides preferably in the fluid/melt phase. Therefore, when employing Th as the internal standard element for determining fluid/melt element concentrations, we obtain maximum element concentrations for the water-free fluid/melt compositions that will be within 20 % of the true values, most likely much better when considering the K_d^{Th} reported by Kessel et al. (2005a). No hydrous or K-bearing minerals were found in the pressure and temperature range of our study (see below). Consequently, the fluid/melt phase is assumed to have a Th/H ratio identical to that of the starting material. The mass of each element in the fluid/melt is then combined with the known mass of H_2O in the experiment in order to determine the composition of the fluid/melt, normalized to 100 wt%.

Phase abundances in all experiments were calculated from anhydrous mass balance constraints based on major element compositions of minerals (Tables S2-5 in supplement), fluid/melt (Table 3), and the bulk composition (Table 1) using a non-weighted least square fit, performing 10,000 runs of Monte Carlo calculations. In each cycle of the calculation, the input numbers are modified within the error range given by the 1 standard deviation of the analyses (a Gaussian error distribution is assumed). The 10,000 sets of results are then collected to statistically evaluate the average and standard deviation of the phase abundance in each experiment. For comparison of phase abundance proportions with increasing *P* and *T*, the above results were normalized to an equal amount of water (15 wt%) in the bulk system.

Results

Run products in this study consist of an anhydrous phase assemblage made of olivine (ol), orthopyroxene (opx), garnet (grt), ±clinopyroxene (cpx), plus an aqueous fluid or hydrous melt phase. Either an aqueous fluid or a hydrous melt is stable in all experiments, indicated by quench solute precipitates present in the diamond trap (Fig. 3d). The phase compositions from subsolidus assemblages for similar systems from Fumagalli et al. (2009), at 1.5–6 GPa and up to 1000 °C, referring to Ti- and Cr-free hydrous lherzolite composition, and from Dvir et al. (2011), at 4–6 GPa and between 700 and 800 °C, referring to K-, Ti-, Cr-free, hydrous lherzolite are compared below. Phase relationships for the lherzolite + water system in all experiments between 700 and 800 °C (Dvir et al. 2011) and between 850 and 1200 °C (this study) are summarized in Fig. 2. Clinopyroxene is absent from the peridotitic assemblage at 1200 °C. The hydrous phase at lower temperatures in K-free compositions is chlorite, which transforms to 10 Å phase with increasing pressure (Dvir et al. 2011; Fumagalli and Poli 2005). In K-bearing hydrous peridotite, phlogopite is the ubiquitous hydrous phase persisting at 3 GPa up to 1000 °C, (Green 1973; Mengel and Green 1989; Thibault and Edgar 1992; Konzett and Ulmer 1999; Conceição and Green 2004; Fumagalli et al. 2009) and at 1.8 GPa up to 1050 °C, in COH–peridotite systems (Tumiati et al. 2013). Neither phlogopite nor other K-bearing mineral phases as equilibrium minerals have been detected in the present experimental charges.

Textural observations and chemical analyses of experimental charges suggest a homogeneous distribution of minerals with no systematic difference in composition of phases along the capsule (Fig. 3a, b). All minerals show a relatively uniform size (10–50 µm) forming sub- to anhedral grains. No zoning within crystals is observed (Fig. 3c). Garnet is typically poikilitic and contains inclusions of clinopyroxene and orthopyroxene (Fig. 3c). Analysis of garnets might therefore be affected as indicated by elevated CaO (especially at lower temperatures of 850–900 °C). Intergrowth of orthopyroxene and clinopyroxene are often observed.

Mineral compositions

Detailed mineral chemistry is given in Tables S2-5 in the supplement. In each experiment, 2–12 individual crystals were analyzed for each mineral. Uncertainties reported throughout this work are 1 standard deviation of n analyses (1σ).

Olivine (Table S2 in the supplement) has Mg# [Mg/(Mg + Fe), molar] of 0.93–0.94 (Fig. 4a), reflecting the bulk composition of the lherzolite. At 6 GPa/1200 °C, in the cpx-free assemblage, the Mg# of the olivine is 0.97. A similar range in Mg# (0.93–0.95) is observed for opx (Table S3), with a slight increase in values with increasing pressure. The opx composition in this study is $En_{90–93}Fs_{5–7}Wo_{0–1}$, with CaO ranging from 0.2 to 0.8 wt%.

Clinopyroxene analyses were normalized to 6 oxygens with all Fe taken as Fe^{2+}, following Cawthorn and Collerson (1974). This procedure results in a minimum Ca-eskolaite ($25A1_{0.5}Ca_{0.5}AlSi_2O_6$) component calculated from cation deficiency. Results are presented in Table S4 and in Fig. 5a. Clinopyroxene at 6 GPa and 1000 °C was observed; however, it was difficult to analyze due to the small grain size. Therefore, for mass balance calculations, the composition of cpx at 1100 °C was taken in all calculations. The compositional range of cpx in the pressure–temperature range of this study is $En_{47–53}Fs_{1–3}Wo_{35–45}$, with Mg# of 0.93–0.94 (Fig. 4a). Clinopyroxene follows a trend of increasing wollastonite and decreasing NaAl or NaCr component with increasing temperature at the expense of enstatite, as already reported by Dvir et al. (2011) and Fumagalli et al. (2009) at subsolidus conditions. The

Table 3 Aqueous fluid and hydrous melt compositions coexisting with lherzolite as obtained in this study

P (GPa)	4					5				6			
T (°C)	850	900	1000	1100	1200	850	1000	1100	1200	900	1000	1100	1200
Exp. #	OC18	OC24	RK307	RK304	RK309	OC26	NV9	RK306	RK311	OC23	RK301	RK300	RK308
n^a	3	3	3	9	5	6	17	7	8	7	10	5	11
Fluid/melt composition (wt%)													
SiO_2	6.68 (1.98)^d	10.57 (0.98)	23.28 (2.30)	34.34 (2.58)	35.05 (1.13)	11.74 (2.90)	14.44 (1.84)	29.83 (2.48)	29.41 (3.04)	5.24 (2.01)	8.61 (1.22)	27.31 (1.09)	31.42 (2.22)
TiO_2	0.07 (0.02)	0.159 (0.003)	0.34 (0.06)	0.24 (0.06)	0.17 (0.05)	0.18 (0.04)	0.11 (0.01)	0.35 (0.03)	0.28 (0.02)	0.04 (0.01)	0.02 (0.01)	0.06 (0.01)	0.28 (0.03)
Al_2O_3	0.58 (0.08)	1.99 (0.13)	2.98 (0.64)	2.91 (0.17)	4.19 (0.67)	1.45 (0.34)	1.43 (0.18)	5.67 (0.55)	4.26 (0.49)	0.13 (0.06)	0.41 (0.04)	1.96 (0.22)	5.18 (0.32)
$Cr_2O_3^b$	–	–	0.2 (0.1)	0.20 (0.05)	0.32 (0.04)	–	–	0.36 (0.04)	0.26 (0.03)	–	0.04 (0.01)	0.07 (0.01)	0.31 (0.03)
FeO^c	0.76 (0.8)	1.86 (0.68)	4.60 (0.50)	4.69 (1.15)	4.56 (0.56)	1.40 (0.33)	3.11 (0.33)	4.07 (0.91)	4.46 (0.68)	0.33 (0.08)	2.46 (0.48)	3.57 (0.43)	4.32 (0.55)
MgO	3.14 (0.57)	5.07 (0.42)	13.88 (0.56)	14.59 (2.62)	17.77 (1.13)	4.81 (1.10)	8.41 (0.69)	12.64 (1.62)	14.90 (1.87)	1.18 (0.40)	5.39 (0.77)	10.12 (0.70)	14.95 (0.93)
CaO	0.07 (0.09)	0.03 (0.05)	7.03 (0.46)	6.07 (0.94)	9.90 (1.37)	2.97 (1.32)	2.61 (0.33)	9.18 (2.67)	14.00 (1.17)	0.56 (0.50)	8.30 (0.94)	9.70 (0.31)	13.99 (1.06)
Na_2O	5.63 (0.57)	5.45 (1.45)	3.35 (1.00)	2.52 (0.26)	2.54 (0.83)	2.92 (0.36)	3.27 (0.43)	3.71 (0.71)	3.04 (0.70)	5.41 (0.66)	4.79 (0.62)	3.87 (0.21)	2.14 (0.21)
K_2O	4.39 (0.29)	3.97 (0.83)	3.02 (0.13)	2.71 (0.22)	2.41 (0.37)	3.63 (0.63)	2.60 (0.51)	3.02 (0.42)	2.50 (0.53)	4.84 (0.63)	4.04 (0.41)	3.55 (0.30)	2.53 (0.27)
H_2O	78.67 (3.04)	70.9 (2.3)	39.4 (1. 7)	28.4 (3.8)	22.3 (1.4)	70.9 (4.4)	63.0 (2.7)	28.6 (3.4)	25.5 (1.8)	82.3 (2.4)	64.4 (1.3)	39.0 (1.0)	24.1 (1.1)
$X\ H_2O^e$	0.93 (0.01)	0.89 (0.01)	0.68 (0.01)	0.57 (0.06)	0.47 (0.03)	0.89 (0.02)	0.85 (0.02)	0.53 (0.03)	0.44 (0.02)	0.92 (0.02)	0.86 (0.03)	0.68 (0.03)	0.53 (0.02)
Anhydrous composition													
SiO_2	31.32	36.32	39.65	50.30	45.57	40.35	40.14	43.34	40.23	29.56	25.26	45.36	41.83
TiO_2	0.33	0.55	0.58	0.35	0.23	0.61	0.32	0.51	0.38	0.23	0.07	0.10	0.37
Al_2O_3	2.74	6.84	5.08	4.26	5.45	4.97	3.97	8.24	5.82	0.73	1.22	3.25	6.90
Cr_2O_3	–	–	0.37	0.29	0.41	–	–	0.52	0.35	–	0.11	0.12	0.42
FeO^c	3.55	6.39	7.84	6.88	5.93	4.81	8.64	5.91	6.11	1.88	7.22	5.93	5.75
MgO	14.73	17.42	23.65	21.36	23.11	16.53	23.37	18.37	20.38	6.67	15.81	16.81	19.90
CaO	0.35	0.11	11.98	8.89	12.87	10.19	7.27	13.34	19.15	3.17	24.37	16.10	18.62
Na_2O	26.40	18.73	5.70	3.69	3.31	10.05	9.08	5.39	4.16	30.51	14.07	6.43	2.84
K_2O	20.58	13.65	5.14	3.97	3.13	12.49	7.22	4.38	3.42	27.26	11.87	5.89	3.37
Element mobility (%)^f													
Si	3 (1)	4 (1)	13 (2)	23 (2)	24 (2)	5 (1)	7 (1)	18 (2)	16 (2)	2 (1)	4 (1)	15 (1)	19 (2)
Ti	15 (4)	35 (1)	109 (21)	93 (25)	67 (18)	44 (11)	31 (3)	120 (15)	87 (7)	8 (2)	6 (2)	19 (2)	98 (10)
Al	2.4 (0.5)	8.3 (0.4)	18 (5)	21 (6)	30 (5)	7 (2)	7 (1)	36 (5)	25 (3)	0.5 (0.2)	1.8 (0.2)	11 (1)	34 (3)
Cr	–	–	9 (4)	10 (3)	16 (2)	–	–	16 (2)	10 (1)	–	1.2 (0.2)	3 (2)	14 (1)
Fe	2.2 (0.2)	6 (2)	20 (3)	24 (6)	24 (3)	5 (1)	12 (1)	19 (5)	19 (3)	0.9 (0.2)	8 (2)	15 (2)	20 (3)
Mg	1.6 (0.3)	2.6 (0.2)	10 (1)	13 (2)	16 (2)	3 (1)	5 (1)	10 (2)	11 (1)	0.6 (0.2)	3.0 (0.4)	7 (1)	12 (1)
Ca	0.4 (0.5)	0.2 (0.3)	54 (6)	57 (9)	93 (15)	18 (8)	17 (2)	77 (24)	105 (10)	3 (2)	48 (6)	72 (3)	119 (11)

Table 3 continued

P (GPa)	4					5				6			
T (°C)	850	900	1000	1100	1200	850	1000	1100	1200	900	1000	1100	1200
Exp. #	OC18	OC24	RK307	RK304	RK309	OC26	NV9	RK306	RK311	OC23	RK301	RK300	RK308
n^a	3	3	3	9	5	6	17	7	8	7	10	5	11
Na	121 (12)	118 (31)	104 (33)	94 (12)	96 (32)	70 (10)	88 (13)	124 (27)	102 (22)	107 (14)	111 (15)	116 (7)	143 (8)
K	127 (9)	116 (24)	126 (12)	137 (14)	122 (21)	117 (22)	94 (19)	136 (24)	102 (22)	128 (17)	126 (13)	143 (13)	117 (13)

[a] Number of analyses along the diamond trap

[b] – Indicates absent from the starting material

[c] All Fe expressed as FeO

[d] Numbers enclosed in parentheses indicate absolute 1 SD, i.e., 6.68(1.98) should be read as 6.68 ± 1.98

[e] X H_2O—mole fraction of H_2O in the fluid or melt phase

[f] Mobility is given as the concentration of an element in the fluid/melt phase multiplied by the fluid/melt abundance in the system divided by its concentration in the bulk system. Values presented are %

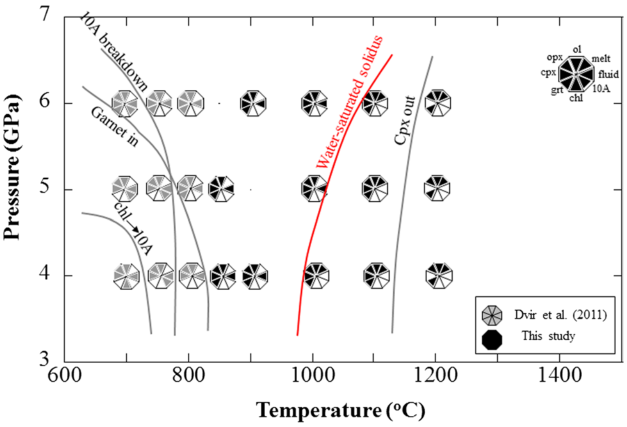

Fig. 2 Pressure–temperature diagram for the K-rich lherzolite + H_2O system. The phases identified in each experiment are shown. For comparison, data below 850 °C are taken from Dvir et al. (2011) (K-poor lherzolite + water). The estimated locations of the two dehydration reactions from Dvir et al. (2011) are shown, as well as the location of the water-saturated solidus found in this study

Al_2O_3 concentration in the cpx decreases with increasing temperature from values of ~3 to ~1 wt%, and the Na_2O concentration decreases with increasing temperature from 1.61 to 0.71 at 4 GPa or 1.65 to 0.82 at 6 GPa. The low Na_2O content is suggested to occur as part of the enhanced leaching of the alkalis into the fluid/melt phase due to high water content in our experiments (up to 20 wt%). At the 4–6 GPa pressure range investigated in this study, clinopyroxene was found to be stable up to 1100 °C and is absent at 1200 °C.

Garnet mineral chemistry is given in Table S5 in the supplement and is illustrated in Fig. 5b. Garnet is mainly pyrope, with compositional ranges of $Pyr_{55–75}Alm_{5–12}Gross_{7–17}$. Only slight changes in composition are observed, showing steadily increasing Mg# from 0.81–0.84 to 0.88–0.93 at all pressures with increasing temperature (Fig. 4a) corresponding to an increase in pyrope component, while the grossular/almandine ratio decreases with increasing pressure. Across the pressure range investigated, majorite fractions are below 1 % and thus insignificant. Both data from Fumagalli et al. (2009) and Dvir et al. (2011) are shown in Fig. 5b for comparison, indicating similar compositions and trends as observed in this study.

At the experimental conditions of this study, the Mg# of the minerals decrease in the sequence cpx > opx = ol > grt, similar to other experimental work (Mengel and Green 1989; Conceição and Green 2004). Similar to experiments by Mengel and Green (1989), no changes in Mg# values are observed in olivine, orthopyroxene, and clinopyroxene while crossing the solidus at each pressure. Only garnet shows an increase in Mg# as crossing the solidus. Both Mengel and Green (1989) and Conceição and Green (2004) reported changes in Mg# of residual phases when hydrous phases are consumed (amphibole, phlogopite, and pargasite). The only change in mineralogy observed in our study is the consumption of clinopyroxene, slightly above the solidus.

The partition coefficient of Fe–Mg between garnet and fluid or melt is between 0.7 and 0.8 throughout the pressure–temperature range of this study, except at low temperatures, at 5 GPa and 850 °C (1.04) and 6 GPa and 900 °C (1.3). These high values most probably reflect disequilibrium crystallization of garnets at low temperatures due to slow diffusivity. Nonetheless, in general, Fe–Mg fractionation between garnet and fluid or melt should be interpreted with caution, because of uncertainties in Fe^{3+}/Fe^{tot} ratios in garnets at high pressures.

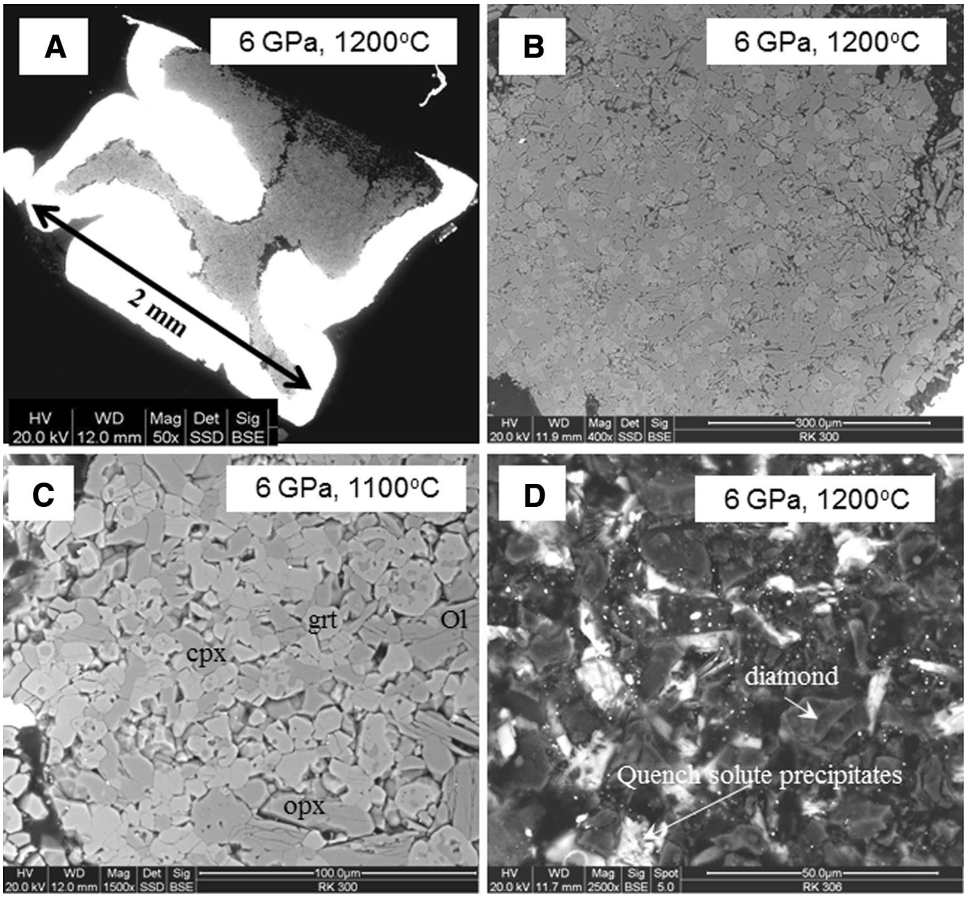

Fig. 3 Backscatter electron images of representative experimental run products. **a** Overview of a half of a capsule of an experiment at 6 GPa and 1200 °C after cutting through the diamond trap. Traces of diamonds (*dark spots*) are observed at the open side of the capsule. **b** Details of the same charge showing homogeneous distribution of the solid phases across the charge. **c** Detailed view of experiment at 6 GPa and 1100 °C showing the lack of zoning in the minerals and the poikilitic texture of the garnets. **d** Detailed view of the diamond trap of experiment at 6 GPa and 1200 °C with quench precipitates in between the diamond aggregates

Aqueous fluid and hydrous melt compositions

The composition of the fluid/melt phase in the range from 850 to 1200 °C and 4–6 GPa is given in Table 3. In each experiment, 3–17 analyses of the diamond trap were performed. The 1 standard deviations on the average amounts of H_2O in the fluid/melt phase range between 1 and 15 %. The H_2O concentration found in this study at 4 GPa and 850–900 °C is 70–79 wt%, corresponding to a mole fraction of H_2O in the liquid of $0.89 < XH_2O < 0.93$ (Fig. 6). This phase is defined as an aqueous fluid. However, at 1000 °C, the H_2O concentration decreases abruptly to 39 wt% ($XH_2O = 0.68$) and then decreases smoothly to 22 wt% ($XH_2O = 0.47$) when temperature increases to 1200 °C. These results indicate a change in the nature of the phase from an aqueous fluid to a hydrous melt. At 4 GPa, Dvir et al. (2011) reported the existence of a fluid phase coexisting with lherzolite, with H_2O concentrations smoothly decreasing from 84 wt% at 700 °C to 67 wt% at 800 °C ($XH_2O = 0.94$ to 0.85). At 5 and 6 GPa, a similar trend is observed, albeit shifted to higher temperature. At 5 GPa, an aqueous fluid phase is stable from 850 °C (with 71 wt% H_2O, $XH_2O = 0.89$) up to a temperature of 1000 °C (with 63 wt% H_2O).The liquid phase found in Dvir et al. (2011) between 700 and 800 °C is a fluid with H_2O concentration decreasing from 87 to 64 wt%. The abrupt decrease in H_2O concentration occurs between 1000 and 1100 °C, from 63 to 28 wt% (XH_2O from 0.85 to 0.53). At 6 GPa, an aqueous fluid phase is stable up to a temperature of 1000 °C with H_2O concentrations smoothly decreasing from 85 wt% at 700 °C (Dvir et al. 2011) to 64 wt% at 1000 °C (XH_2O from 0.95 to 0.86). The stepwise decrease in H_2O concentration occurs between 1000 and 1100 °C, from 64 to 38 wt% (XH_2O from 0.86 to 0.68).

A major change in composition across the step in H_2O concentration is observed for most element oxides (Fig. 7). SiO_2, Al_2O_3, MgO, FeO, and CaO concentrations increase dramatically, while Na_2O and K_2O concentrations decrease with increasing temperature. These changes are also shown in the element mobility given in Table 3, albeit with sometimes large uncertainties in the values. The mobility of the elements in the fluid/melt phase is defined as the percentage of the oxide in the starting material that resides in the fluid/melt phase at the experimental conditions. Most elements drastically increase their mobility as H_2O concentration in the fluid/melt sharply drops. At higher temperatures, the mobility of SiO_2 and Al_2O_3 increases with increasing temperature, whereas the mobility of FeO and MgO is

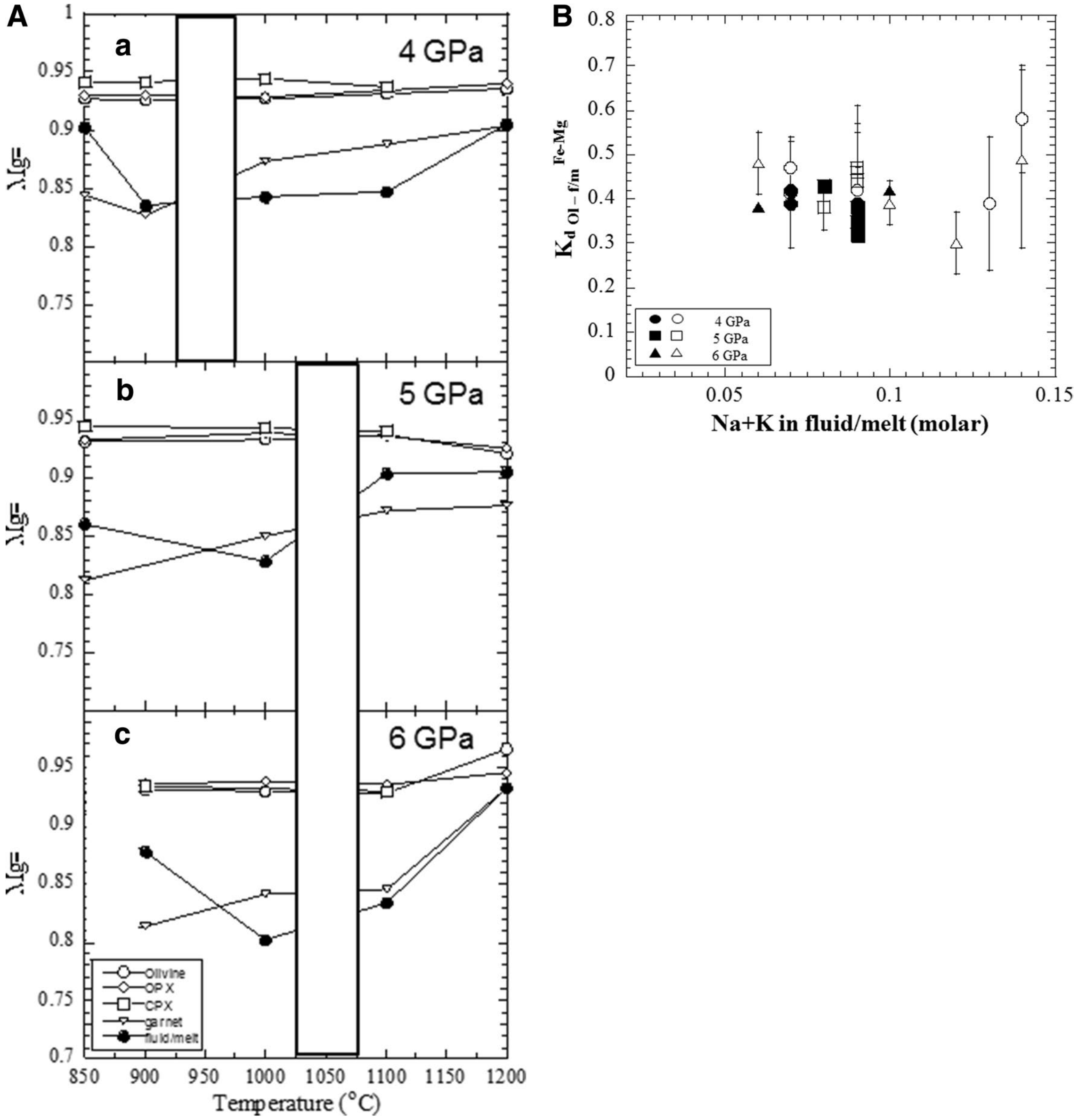

Fig. 4 **a** Variation in the Mg# of the solid phases as well as the fluid/melt phase as a function of temperature at each pressure investigated. The location of the water-saturated solidus is shown as *white bands*. **b** The predicted and measured Fe–Mg equilibrium values between olivine and fluid/melt ($K_d{}^{\text{Fe–Mg}}_{\text{Ol–f/m}}$) for each experiment as a function of molar Na + K content in the fluid or melt phase (on anhydrous basis). *Open symbols* measured values. *Filled symbols* predicted values based on the equation given by Toplis (2005)

constant within error. The mobility of Na_2O and K_2O is close to 100 % within 1 SD throughout the temperature range investigated.

Discussion

Approach to equilibrium

Because the starting material was a synthetic amorphous gel, the resulting mineral assemblage indicates a complete conversion of the starting powder to high-pressure phases at pressure–temperature–duration of the experiments. All phases are homogeneously distributed throughout the capsule; no gradients in modal abundances and no intragrain zoning are observed (Fig. 3a–d). Triple junctions between minerals are often observed throughout the capsule (Fig. 3c). These observations point to a high degree of equilibrium in the experiments. In order to further verify the degree of equilibrium achieved during the experiments, we applied the thermometer based on the Ca content in orthopyroxene calibrated between 1 and 6 GPa and

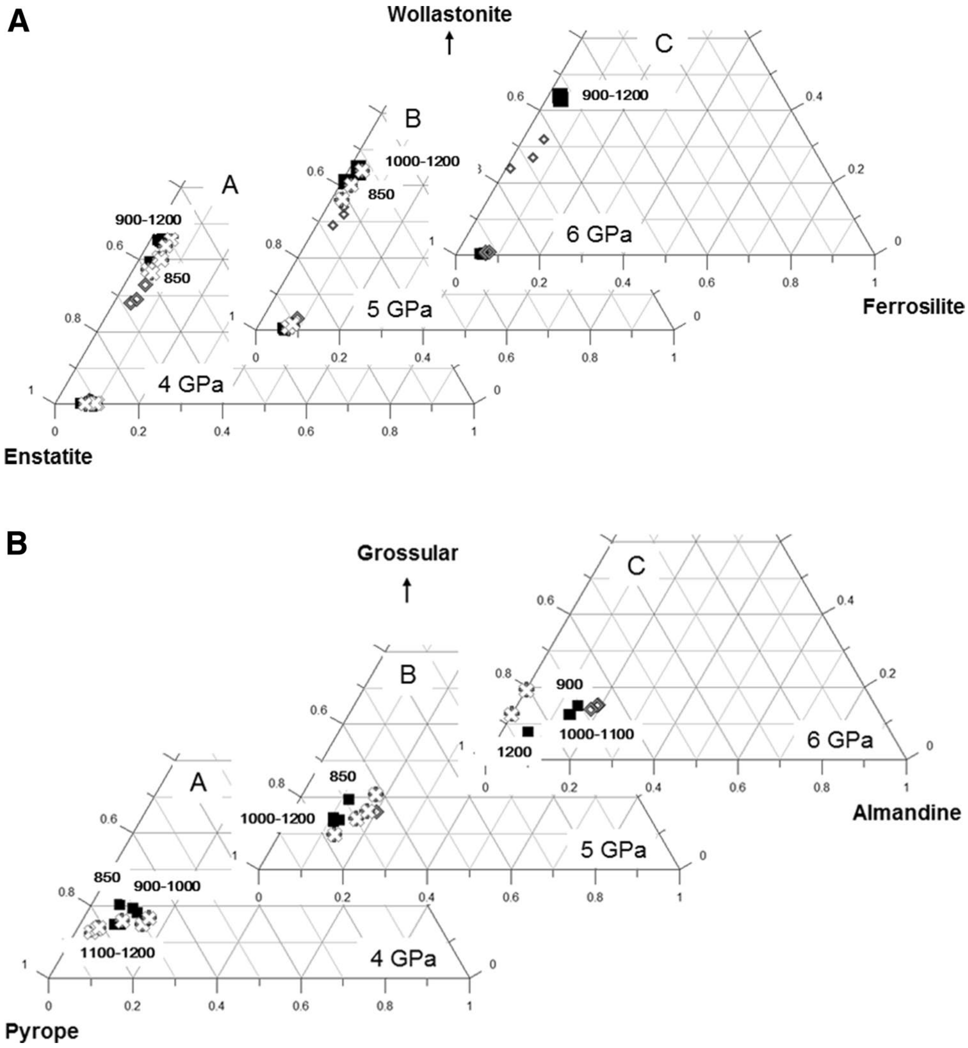

Fig. 5 **a** Ternary enstastite ($MgSiO_3$)–ferrosilite ($FeSiO_3$)–wollastonite ($CaSiO_3$) diagram for pyroxene compositions in the K–lherzolite–H_2O experiments in this study. For comparison, subsolidus data in *gray diamonds* are taken from Dvir et al. (2011) and in *black crosses* are taken from Fumagalli et al. (2009). *Numbers* adjacent to *symbols* indicate the temperature. **b** Ternary pyrope ($Mg_2Al_2Si_3O_{12}$)–almandine ($Fe_3Al_2Si_3O_{12}$)–grossular ($Ca_3Al_2Si_3O_{12}$) diagram for garnet compositions in K–lherzolite–H_2O experiments in this study. For comparison, subsolidus data in *gray diamonds* are taken from Dvir et al. (2011) and in *gray crosses* are taken from Fumagalli et al. (2009). *Numbers adjacent to symbols* indicate the temperature, only for the present study

900 to 1400 °C for natural, dry lherzolite compositions (Brey and Kohler 1990). Comparison of temperatures recorded for the center of the capsule with those obtained from thermometry (Table 4) agrees well at temperatures below 1100 °C; above 1100 °C, calculated temperatures are always lower, by up to 90 °C, than experimental temperatures.

Another way of examining the equilibrium in our experiments is assessing the Fe–Mg exchange coefficient between olivine and fluid/melt, $K_{\mathrm{d\ Ol–f/m}}^{\ \mathrm{Fe–Mg}}$ (defined as the molar Fe^{2+}/Mg of the olivine divided by the same ratio in the fluid or melt). The measured values in our study are between 0.38 and 0.58 (Fig. 4b). The exchange coefficients were found to be 0.3 at low pressures (Roeder and Emslie 1970). However, studies have shown that it increases with pressure to ~0.34–0.35 at 6 GPa (Ulmer 1989; Toplis 2005). No obvious systematic changes in the exchange coefficients are observed with pressure, temperature, or composition (water content or alkali content). An exception is two experiments at 4 GPa (850 and 900 °C) and two at 6 GPa (900 and 1000 °C) with the highest alkali content in the fluid or melt phase (molar fraction of Na + K on anhydrous basis). An increase in exchange coefficient is observed with increasing alkali content.

Toplis (2005) derived a thermodynamic expression of the exchange coefficient $K_{\mathrm{d\ Ol–f/m}}^{\ \mathrm{Fe–Mg}}$ taking into account the composition of the olivine as well as that of the fluid or melt and the pressure and temperature of equilibrium. Applying Toplis (2005) model to the olivine and fluid or melt compositions at each pressure and temperature yields exchange coefficients in the range of 0.32–0.43. Comparison of the exchange coefficients determined in each experiment with those calculated using Toplis (2005) model is shown in Fig. 4b. Most experiments fall close to the predicted values or agree with the predicted values within analytical uncertainties. The exchange coefficients for the four experiments with high alkali content cannot be calculated using the Toplis (2005) model.

All the above reasoning indicates that the capsules in this study approached equilibrium during the experiments

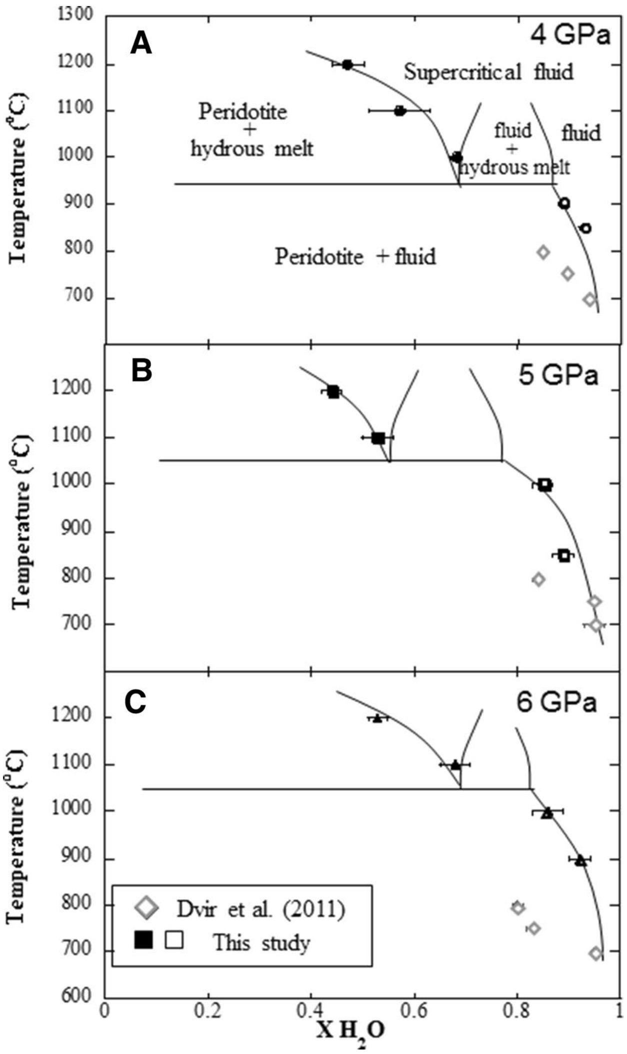

Fig. 6 Changes in H_2O concentration of the liquid phase [$X(H_2O)$], given as the mole fraction of H_2O in the liquid, as a function of temperature at each pressure investigated. The data at temperatures between 700 and 800 °C are taken from Dvir et al. (2011) in gray; these refer to K-, Ti-, and Cr-free lherzolite–water system investigated at 4–6 GPa and 700–800 °C. Superimposed on the data are schematic locations of the solidi and liquidi at each pressure. The various fields are labeled in (**a**). *Open symbols* subsolidus experiments. *Filled symbols* supersolidus experiments. *Gray symbols* represent experiments by Dvir et al. (2011). *Black symbols* represent experiments in this study

and, therefore, the results are meaningful in quantifying the peridotite–water system at high pressures and temperatures.

Solid phase assemblages

The minerals found in experiments in this study are an anhydrous assemblage of olivine–orthopyroxene–garnet ± clinopyroxene. Both Fumagalli et al. (2009) and Konzett and Ulmer (1999), who studied similar K–lherzolite compositions at similar P–T conditions, reported on the stability of phlogopite in the solid phase. Detailed XRD and SEM examinations of the run products in this study reveal that phlogopite is absent from the solid assemblage, but it is present in the diamond trap, and only there, as part of the fluid/melt phase quench products. Analyses of the phlogopite grains found in between the diamond grains were performed on the SEM using qualitative EDS analyses normalized to 100 % on an anhydrous basis. The composition of the phlogopite is characterized by low Mg# (0.85–0.91) and high SiO_2 (50–54 wt%) and FeO (4.4–6.7 wt%). These compositions further support our conclusion that the phlogopite is a quench phase and not a primary phase (Mengel and Green 1989; Conceição and Green 2004). The absence of phlogopite from the mineral paragenesis of the lherzolite in our experiments is interpreted to be the result of the high bulk water fraction (14–20 wt % but one run; set on purpose to ensure that only fluid phase fills the voids in the diamond trap) compared to previous studies on similar bulk rock composition (Konzett and Ulmer 1999; Fumagalli et al. 2009). Low water concentrations thus favored the stability of low-melting components, such as hydrous minerals [water fraction loaded by Fumagalli et al. (2009): 1.8–16 wt%; Konzett and Ulmer (1999): <2 wt%]. Higher water concentrations in our experiments allowed for preferred dissolution of K_2O (and Na_2O), which are essential for the stability of phlogopite, to the aqueous fluid or hydrous melt phase, rendering the hydrous mineral unstable. A similar phenomenon was observed by Green et al. (2010, 2014) regarding the hydrous pargasite phase and used as explanation for lack of amphibole in the mineral assemblage of a fertile lherzolite with H_2O concentration >~5 wt% at pressure and temperature conditions where amphibole was stable at lower water contents; i.e., at 2.5 GPa, 1000 °C.

Aqueous fluid and hydrous melt compositions

At given *P*, the mobile phase evolves toward higher total dissolved solids with increasing *T* and each of these trends reveals one abrupt change from 71 to 40 wt% H_2O at 4 GPa between 900 and 1000 °C, from 63 to 29 wt% at 5 GPa between 1000 and 1100 °C, and from 64 to 39 wt% at 6 GPa between 1000 and 1100 °C. These jumps, corresponding to nearly a doubling in total dissolved solids, are thus interpreted to locate the water-saturated solidus of K-bearing lherzolite, showing total dissolved solids loads characteristic for aqueous fluid below and for hydrous melts above the respective temperatures (Fig. 6). These jumps are further characterized by mostly abrupt compositional changes (Fig. 7).

The aqueous fluids as well as the hydrous melts are all peralkaline, olivine–feldspathoid in nature nepheline/leucite–kalsilite–acmite–normative. The K/Na (molar) ratios

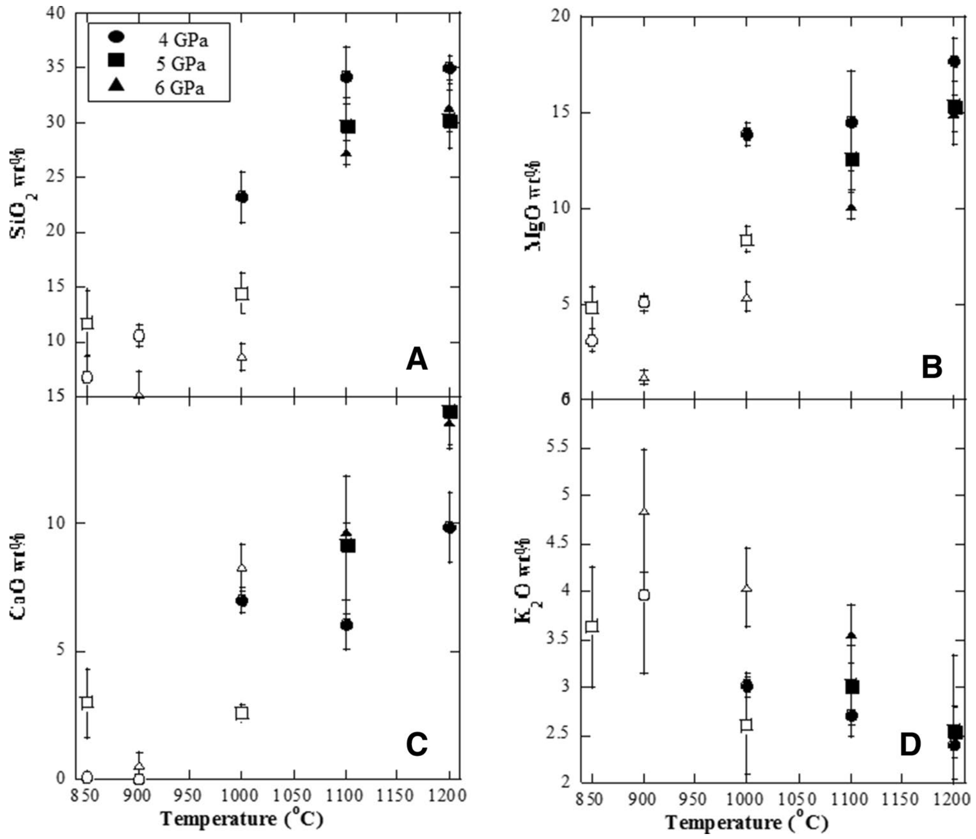

Fig. 7 Fluid and melt composition–temperature diagrams for SiO_2, MgO, CaO, and K_2O (in wt% absolute concentrations) in K–lherzolite–H_2O experiments in this study. *Open symbols* subsolidus experiments. *Filled symbols* supersolidus experiments

of the fluid/melt range between 0.48 and 0.82 from a bulk composition of 0.49. This is consistent with leaching all the potassium into the fluid/melt phase at all temperatures but the partial leaching of sodium. Part of the sodium is still retained in clinopyroxene as long as it is stable as a residual mineral. Similar degree of undersaturation and K/Na ratio were also found by Mengel and Green (1989).

The location of the water-saturated solidus of lherzolitic peridotite

It is clear that the composition of a peridotite exert a prominent influence on the location of its water-saturated solidus. Variations in major element concentrations dictate variations in mineral modal abundances. Variations in minor and trace element concentrations influence the stability of minor minerals, for example phlogopite in K-bearing systems. The composition of the fluid or melt coexisting with the peridotite will change accordingly, and the location of the water-saturated solidus may shift somewhat in *T* at given *P*. However, even for similar mantle compositions, the literature results still do not agree with each other, with proposals ranging over several hundred degrees C in the pressure range investigated here (Fig. 1).

Most of the existing water-saturated solidus determinations refer to alkali-poor lherzolite systems (containing 0.33–0.66 wt% Na_2O and 0.03–0.13 wt% K_2O). The results cluster in two major groups. The water-saturated solidi of Kushiro et al. (1968), Green (1973), and Millhollen et al. (1974) are curved concave up temperature with a minimum melting temperature of about 970 °C at pressures of 1.5–2 GPa. The H_2O content in the three studies is less than 6 wt %. Mysen and Boettcher (1975) and Grove et al. (2006) suggested a solidus with a minimum of about 800 °C around 3 GPa. Till et al. (2012a, b, c) extended Grove et al. (2006) experiments and proposed the extension of the solidus between 3.2 and 6 GPa to be at 810 °C. The solidi locations in the latter studies agree well with each other, but these experiments used very high water/rock ratios and leached alkali elements and silica, from the lherzolite into the fluid/melt phase (Green et al. 2010, 2014). Recently, Green et al. (2010, 2014) reported that the first melt of an alkali-poor lherzolite (model upper mantle/MORB-source composition) peridotite with 1.45 wt% H_2O at 1.5 GPa appears at 970 °C, increasing through 1025 °C at 2.5 GPa, 1225 °C at 4 GPa and 1375 °C at 6 GPa. Spandler et al. (2014) observed aqueous fluid inclusions trapped in olivine (an aqueous fluid in equilibrium with harzburgite) at 900 °C and 4 GPa, thus demonstrating the absence of a hydrous melt at these conditions.

The starting material used in the current study is characterized by significant alkali concentrations of 0.86 wt%

Table 4 Modal phase abundance in K-rich lherzolite–water experiments

P (GPa)	4						5			6			
T_{th} (°C)[a]	850	900	1000	1100	1200	850	1000	1100	1200	900	1000	1100	1200
T_{hs} (°C)[b]	865	922	1017	1083	1216	867	1020	1115	1217	917	1000	1120	1200
T_{Brey} (°C)[c]	927	990	1028	1001	1129	843	1034	1058	1128	891	909	1065	1129
Total capsule phase abundance (in wt. fractions)[d]													
Ol	0.35 (0.05)[e]	0.36 (0.02)	0.43 (0.03)	0.31 (0.05)	0.26 (0.02)	0.29 (0.03)	0.32 (0.03)	0.22 (0.03)	0.26 (0.02)	0.33 (0.02)	0.26 (0.01)	0.31 (0.01)	0.23 (0.02)
OPX	0.21 (0.05)	0.22 (0.03)	0.16 (0.03)	0.21 (0.05)	0.30 (0.03)	0.29 (0.04)	0.23 (0.04)	0.35 (0.04)	0.35 (0.03)	0.23 (0.02)	0.34 (0.02)	0.27 (0.2)	0.35 (0.03)
CPX	0.06 (0.01)	0.08 (0.01)	0.01 (0.01)	0.02 (0.02)	–[e]	0.05 (0.02)	0.06 (0.01)	0.02 (0.03)	–	0.09 (0.01)	0.04 (0.01)	0.01 (0.01)	–
Grt	0.19 (0.01)	0.16 (0.01)	0.13 (0.02)	0.13 (0.01)	0.11 (0.01)	0.16 (0.01)	0.16 (0.01)	0.12 (0.01)	0.13 (0.01)	0.18 (0.01)	0.172 (0.004)	0.156 (0.004)	0.13 (0.01)
Fluid	0.187 (0.004)	0.187 (0.002)	–	–	–	0.21 (0.01)	0.23 (0.01)	–	–	0.17 (0.01)	0.20 (0.01)	–	–
Melt	—[f]	–	0.27 (0.02)	0.32 (0.03)	0.32 (0.03)	–	–	0.29 (0.03)	0.26 (0.03)	–	–	0.26 (0.01)	0.30 (0.01)

Ol olivine, *CPX* clinopyroxene, *OPX* orthopyroxene, *Grt* garnet

[a] T_{th}—Thermocouple readings

[b] T_{hs}—Thermocouple readings corrected for position of the middle of the capsule assuming a gradient of 11 °C/mm (Konzett et al. 1997)

[c] T_{Brey}—Temperature calculated using the Ca content in opx (Brey and Kohler 1990). Estimated uncertainties are ±15 °C

[d] Modal phase abundances in weight fractions (normalized to constant 15 wt% H_2O in the bulk system) calculated by Monte Carlo mass balance calculations

[e] –Numbers enclosed in parentheses indicate absolute 1 standard deviation, i.e., 0.35(0.05) should be read as 0.35 ± 0.05

[f] –Indicates absent from the run product assemblage

Na_2O and 0.64 wt% K_2O. Determinations of the water-saturated solidus for alkali-rich lherzolite (phlogopite-bearing lherzolite) are scarce. Green (1973) performed experiments with 6 and 1.2 wt % H_2O and determined a curved concave up solidus with a minimum melting temperature of about 970 °C at a pressure of 1.5 GPa. Mengel and Green (1989) and Conceição and Green (2004) located the water-saturated solidus for phlogopite-bearing lherzolite with 1 wt% H_2O at 1050 °C at 1.5 GPa. Thibault Edgar (1992) added 0.23 wt% H_2O to the bulk lherzolite composition and defined the solidus at 1175 °C at 3 GPa. Our experimental results for a system containing 8–20 wt% H_2O is located between 900 and 1100 °C at 4–6 GPa.

Elevated alkali concentration is known to lower the temperature of the solidus by a few tens of degrees. This was also observed in basaltic systems [e.g., Schmidt et al. (2004) vs. Kessel et al. (2005a, b)]. Increasing water content was shown to lower the temperature of the water-saturated solidus as well, as long as leaching effect is negligible. Green et al. (2010, 2014) have demonstrated that the water/rock ratio strongly influences the phase stability of the residual phases in the peridotite–water system; the higher the water content, the more refractory the residual mineral assemblage, because less refractory phases are leached into the fluid/melt phase. As a consequence, as water content increases, the location of the water-saturated solidus is shifted to higher temperature.

The water-saturated solidus of an alkali-rich lherzolite + H_2O system determined here lies at a slightly lower temperature (~60 °C at 4 GPa) than the solidus of the K-poor peridotite–H_2O system determined by Kushiro et al. (1968) at similar pressures (Fig. 1), which we attribute to result from the higher alkali element concentrations in our starting material. The solidus is located slightly at lower temperature to the extrapolation of the solidi of Mengel and Green (1989) and Conceição and Green (2004) for alkali-rich lherzolite, probably due to higher alkali contents in our study.

In addition to the differences in solidi location due to composition, differences in the location of the water-saturated solidus can also be attributed to technical and analytical difficulties in identifying the fluid vs. melt phase. The primary hurdle in locating the beginning of melting is the difficulty in reliably identifying and quantifying the composition of the melt phase in the run product, because high-pressure liquids are unquenchable. Being one homogeneous phase at run P and T, the fluid or melt phase undergoes silicate exsolution during quenching, producing a mixture of water-rich liquid and precipitates. After quenching the experiments, Grove et al. (2006) and Till et al. (2012a) pierced the capsules, allowing the water containing some dissolved solids at room temperature to escape before polishing the capsules for analysis. The existence of melt vs. fluid was then inferred based on textural characterization of quench solids only, such as the appearance of interstitial silicate blebs. Similar blebs were reported to represent experimental quench solutes from aqueous fluids by Aerts et al. (2010). Silicate solids in olivine-hosted aqueous fluid inclusions reported by Spandler et al. (2014) represent daughter crystals formed upon fluid inclusion cooling to room temperature.

Because of such textural ambiguities, it is claimed here that compositional systematics of the fluid/melt phases are the most reliable way to identify the presence of hydrous melt or aqueous fluid in an experimental run product brought to ambient P and T. As stated by Kessel et al. (2004), Green et al. (2010), and Stalder (2012), the identification of fluid vs. melt based on textural observations alone can be misleading. Location of the water-saturated solidus in this work is revealed by a sharp decrease in the H_2O concentration of the liquid phase between 900 and 1000 °C at 4 GPa, and between 1000 and 1100 °C at 5 and 6 GPa (Fig. 6), that goes along with a drastic jump in composition of the solute load (Fig. 7). In Fig. 6, schematic solidus and liquidus curves are superimposed on the experimental liquid compositions. As expected, the location of the solidus is shifted to higher H_2O concentrations with increasing pressure toward the second critical endpoint.

In fact, when considering the distinctive changes in mineral chemistry close to 1000 °C reported by Till et al. (2012a, b, c), it becomes evident to us, as well as to Stalder (2012) and Green et al. (2012) that their location of the solidus at 800 °C is incorrect. Their results are most consistent with transition across the water-saturated solidus at 1000 °C, consistent with the results presented here and in Spandler et al. (2014). Moreover, their stated melt fraction also increases significantly at around 1000 °C, a necessary consequence upon transition across the water-saturated solidus in a closed system with fixed water-to-silicate mass ratio (compare Fig. 6). It thus follows that the direct determination of the liquid phase compositions is the most reliable way to locate the solidus of a system. By the use of diamond-trap experiments [developed by Baker and Stolper (1994) and Kushiro and Hirose (1992)] analyzed by cryogenic LA-ICP-MS techniques [developed by Kessel et al. (2004) and refined by Aerts et al. (2010)], the chemical composition of the fluid or melt phase is measured directly. No textural implications other than identification of the position of the diamond aggregate layer in the run product are involved in this technique. Dvir et al. (2011) directly determined the fluid composition at 4 GPa/800 °C and found H_2O concentrations of 67 wt%, inferred to represent an aqueous fluid with 33 wt% dissolved load. Synthetic aqueous fluid inclusions trapped in olivine at 900 °C/4 GPa texturally document the presence of an aqueous fluid in a natural harzburgite at these conditions (Spandler et al.

2014). Clearly, quenching such an aqueous fluid to ambient temperatures will produce quench precipitates that may look texturally similar to quenched hydrous melt [see, e.g., Aerts et al. (2010) for an illustration], or it produces the daughter minerals in fluid inclusions illustrated in Spandler et al. (2014) and sometimes observed in the diamond trap, e.g., phlogopite in our case.

Second critical endpoint in peridotitic compositions

Constraining the location of the water-saturated solidus of a peridotite composition covering significant portions of the Earth's upper mantle also requires locating its termination at the second critical endpoint. Below the pressure and temperature of the second critical endpoint, both hydrous melts as well as aqueous fluids can be stable with mantle rocks. Above these P–T conditions, one supercritical liquid phase exists. In spite of the importance of the exact location of the second critical endpoint in modeling elemental mobility and affinity [compare data in Kessel et al. (2005a, b)], little is known about its position in the peridotite–water system. Melekhova et al. (2007) determined the composition of liquids in the MgO–SiO$_2$–H$_2$O (MSH) system between 11 and 13.5 GPa and identified the second critical endpoint to be at 11 GPa and 1100 °C. This is consistent with Stalder et al. (2001) who reported that below 10.5 GPa, a wet solidus still persists. Studying the MSH system provides limited understanding of the mantle behavior as only Mg end-member minerals are considered. Addition of elements such as Fe, Ca, Al, and Na to the bulk starting composition results in profound effects on phase equilibria and stabilities [e.g., Wallace and Green (1991)]. Many high-pressure phases are solid solutions (olivine, pyroxene, garnet, mica), resulting in continuous reactions that affect the liquid composition in equilibrium with solid residue over a wide range in pressure and temperature. Mibe et al. (2007) determined the second critical endpoint of a close-to-natural peridotite–H$_2$O system to be at 3.8 GPa and 1000 °C, performing multi-anvil experiments and employing X-ray radiography technique. They run capsules containing 40–60 wt% H$_2$O (compositions below the solvus) and imaged the transition from two liquids (aqueous fluid and hydrous melt) to one liquid (supercritical liquid) while heating. However, since the shape of the solvus in P–T–X phase diagram of the peridotite–water system is unknown, it is not clear which path the peridotite–H$_2$O system of Mibe et al. (2007) had experienced during heating and pressurizing (because the system follows its isochore). Moreover, a second critical endpoint for water-saturated peridotite that is lower than that for water-saturated basalt is inconsistent with expectations derived from incompatibility considerations, e.g., that the solidus of fertile compositions is lower than that of their refractory counterparts. Our data at 4–6 GPa reveal a compositional jump in H$_2$O as well as in all other oxides which we interpret to represent transition across the water-saturated solidus. Therefore, we suggest that the second critical endpoint is located above 6 GPa in the water-saturated K-rich peridotite system.

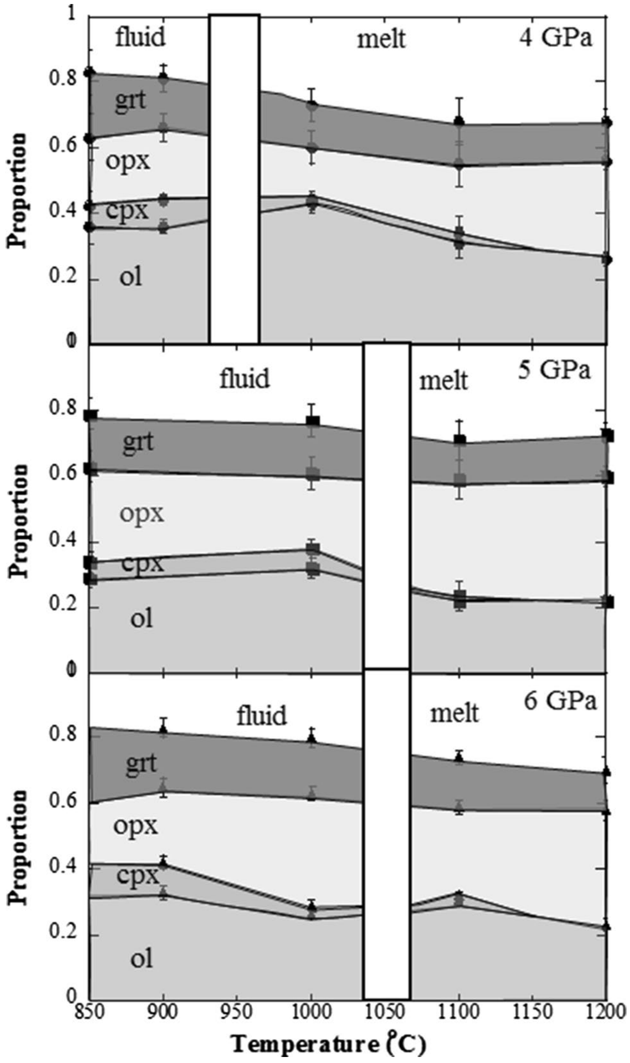

Fig. 8 Modal abundances (in wt%) of the solid and liquid phases obtained through mass balance calculations as a function of temperature at each pressure investigated in this study. Phase abundances plotted on the *Y* axis are cumulative. The location of the water-saturated solidus is shown as *white bands*

Phase abundances and melting reactions

Phase abundances at each P–T are obtained through mass balance calculations (Table 4) and are illustrated in Fig. 8 (cumulative wt. fractions). The calculations were performed for an equal amount of H$_2$O (15 wt%) in the system, to ease comparability of the dataset. Olivine and opx are the most abundant minerals in the solid throughout the investigated temperature interval. At all pressures, the amount of olivine in the peridotite + H_2O system decreases from 30–40 % to 20 % with increasing temperature, while the amount of opx increases from ~20 % to 30–40 %. The clinopyroxene amounts to 5–10 % of the system at lower temperatures, decreasing with increasing temperature until it is consumed completely at 1200 °C at all pressures investigated. The modal amount of garnet amounts to ~20 % of the system, slightly decreasing with increasing temperature. The fluid/melt phase increases its weight fraction with increasing temperature. At 4 GPa, the aqueous fluid fraction at temperatures of 850–900 °C is 18 %. Upon crossing the solidus, the hydrous melt fraction at 1000 °C is 27–32 %. At 5 GPa, the amount of aqueous fluid phase is 21–23 % below 1000 °C, while the amount of hydrous melt at 1100 °C is 29 %. At 6 GPa, the amount of aqueous fluid phase is 17–20 % below 1000 °C, while the amount of hydrous melt at 1100 °C is 26–30 %.

These observations can be transformed into the melting reaction based on phase abundances. A similar reaction is found at 4 GPa (between 1000 and 1200 °C), at 5 GPa (between 1100 and 1200 °C), and at 6 GPa (between 1000 and 1100 °C):

(1) olivine + clinopyroxene + garnet = melt + orthopyroxene

The large errors on the reaction coefficients due to the large errors in the modes, especially of the fluid/melt phase, allow us to present only a general reaction. At all pressures, olivine, clinopyroxene, and garnet in the peridotite coexisting with aqueous fluid phase are consumed to form a hydrous melt and orthopyroxene. The composition of the olivine, orthopyroxene, and garnet does not change significantly during melting (Fig. 5b) while clinopyroxene composition changes during melting, as Na_2O, Al_2O_3, FeO, and MgO concentrations decrease while CaO concentration increases with increasing temperature (Fig. 5a; Table S3). This suggests a preferential dissolution of the enstatite and ferrosilite components into the melt, enriching the clinopyroxene in the wollastonite component. Within uncertainties, all the K resides in the fluid or melt phase throughout the temperature and pressure range of this study, consistent with the lack of a K-rich mineral such as phlogopite in the residual peridotite. The mobility of Fe and Mg increases from 1 to 5 % at low temperatures to 20 % above the solidus at all pressures, increasing only slightly as temperature increases further. While the mobility of Si at low temperatures increases with increasing pressure, it decreases with increasing pressure at higher temperature. This behavior corresponds to the enrichment of the residual peridotite in opx and depletion in olivine. The mobility of Ca and Al is very low at low temperatures. It increases significantly with increasing temperatures due to the consumption of clinopyroxene into the hydrous melt phase.

At 4 GPa and 900 °C, the fluid amounts to 19 wt% of the system. At 1000 °C, there are 27 wt% of melt, i.e., an increase of 9 wt%. If 950 °C is taken as the solidus temperature, then at 4 GPa, this corresponds to melt productivity of 0.18. If solidus is taken at 910 °C, then the productivity is 0.1. With increasing temperature, the isobaric melt productivity decreases to 0.03. Similarly at 5 and 6 GPa, the initial melt productivity 50 degrees above the solidus is 0.12, decreasing to 0.04. These values are similar to those found for other hydrous systems (Gaetani and Grove 1998; Hirschmann et al. 1999; Ulmer 2001; Till et al. 2012a, b, c).

Acknowledgments This work was supported by Israel Science Foundation Grants (251/09). Vitali Gutkin and Dr. Vladimir Uvarov from the Nano-characterization Center at the Hebrew University are thanked for their help with the SEM and XRD work. Omri Dvir is thanked for his help with the LA-ICP-MS analyses. Judah Coddington and Noga Vaisblat are thanked for their help in the experimental work. We appreciate the very valuable comments of D.H. Green and two anonymous reviewers, and the excellent comments and editorial work of John Blundy and Othmar Müntener, helping us to significantly improve the manuscript.

References

Aerts M, Hack AC, Reusser E, Ulmer P (2010) Assessment of the diamond-trap method for studying high pressure fluids and melts and an improved freezing stage design for laser ablation ICP-MS analysis. Am Mineral 95:1523–1526

Ayers J (1998) Trace element modeling of aqueous fluid–peridotite interaction in the Brey GP Kohler T (1990) Geothermobarometry in four-phase lherzolite: I. Experimental results from 10 to 60 kb. J Petrol 31:1313–1352

Baker MB, Stolper EM (1994) Determining the composition of high-pressure mantle melts using diamond aggregates. Geochim Cosmochim Acta 58:2811–2827

Brey GP, Kohler T (1990) Geothermobarometry in four-phase lherzolite II. New thermobarometers, and practical assessment of existing thermobarometers. J Petrol 31:1313–1352

Cawthorn RG, Collerson KD (1974) The recalculation of pyroxene end-member parameters and the estimation of ferrous and ferric iron content from electron microprobe analyses. Am Mineral 59:1203–1208

Conceição RV, Green DH (2004) Derivation of potassic (shoshonitic) magmas by decompression melting of phlogopite + pargasite lherzolite. Lithos 72:209–229

Dvir O, Pettke T, Fumagalli P, Kessel R (2011) Fluids in peridotite-water system up to 6 GPa and 800°C: new experimental constrains on dehydration reactions. Contrib Mineral Petrol 161:829–844

Fedortchouk Y, Canil D, Semenets E (2007) Mechanisms of diamond oxidation and their bearing on the fluid composition in kimberlite magmas. Am Mineral 92:1200–1212

Fedortchouk Y, Matveev S, Carlson JA (2010) H_2O and CO_2 in kimberlitic fluid as recorded by diamonds and olivines in several Ekati diamond mine kimberlites, Northwest Territories, Canada. Earth Planet Sci Lett 289:549–559

Fumagalli P, Poli S (2005) Experimentally determined phase relations in hydrous peridotites to 6.5 GPa and their consequences on the dynamics of subduction zones. J Petrol 46:555–578

Fumagalli P, Stixrude L, Poli S, Snyder D (2001) The 10Å phase: a high-pressure expandable sheet silicate stable during subduction of hydrated lithosphere. Earth Planet Sci Lett 186:125–141

Fumagalli P, Zanchetta S, Poli S (2009) Alkali in phlogopite and amphibole and their effects on phase relations in metasomatized peridotites: a high pressure study. Contrib Mineral Petrol 158:723–737

Gaetani AG, Grove TL (1998) The influence of water on melting of mantle peridotite. Contrib Mineral Petrol 131:323–346

Green DH (1973) Experimental melting studies on a model upper mantle composition at high pressure under water-saturated and water-undersaturated conditions. Earth Planet Sci Lett 19:37–53

Green DH, Hibberson WO, Kovacs I, Rosenthal A (2010) Water and its influence on the lithosphere–asthenosphere boundary. Nature 467:448–452

Green DH, Rosenthal A, Kovacs I (2012) Comment on "The beginnings of hydrous mantle wedge melting", CB Till, TL Grove, AC Withers, Contrib Mineral Petrol 164:1077–1081. doi 10.1007/s00410-011-0692-6

Green DH, Hibberson WO, Kovacs I, Rosenthal A, Kovacs I, Yaxley GM, Falloon TJ, Brink F (2014) Experimental study of the influence of water on melting and phase assemblages in the upper mantle. J Petrol 55:2067–2096

Grove TL, Chatterjee N, Parman SW, Medard E (2006) The influence of H_2O on mantle wedge melting. Earth Planet Sci Lett 249:74–89

Guillong M, Meier DL, Allan MM, Heinrich CA, Yardley BWD (2008) Sills: a matlab-based program for the reduction of Laser Ablation ICP-MS data of homogeneous materials and inclusions. Mineral Assoc Can 40:328–333 Short course series

Hamilton DL, Henderson CMB (1968) The preparation of silicate composition by gelling method. Mineral Mag 36:832–838

Hirschmann MM, Asimow PD, Ghiorso MS, Stolper EM (1999) Calculation of peridotite partial melting from thermodynamic models of minerals and melts. III. Controls on isobaric melt production and the effect of water on melt production. J Petrol 40:831–851

Jochum KP, Weis U, Stoll B, Kuzmin D, Yang Q, Raczek I, Jacob D, Stracke A, Birbaum K, Frick DA, Günther D, Enzweiler J (2011) Determination of reference values for NIST SRM 610–617 glasses following ISO guidelines. Geostand Geoanalytical Res 35:397–429

Kägi R, Müntener O, Ulmer P, Ottolini L (2005) Piston-cylinder experiments on H_2O undersaturated Fe-bearing systems: an experimental setup approaching fO_2 conditions of natural calc-alkaline magmas. Am Mineral 90:708–717

Keppler H, Audétat A (2005) Fluid-mineral interaction at high pressure. In: Miletich A (ed) Mineral behavior at extreme conditions, vol 7. EMU Notes in Mineral. Eötvös University Press, Budapest, pp 225–252

Kessel R, Ulmer P, Pettke T, Schmidt MW, Thompson AB (2004) A novel approach to determine high-pressure, high-temperature fluid and melt compositions using diamond-trap experiments. Am Mineral 89:1078–1086

Kessel R, Schmidt MW, Ulmer P, Pettke T (2005a) Trace element signature of subduction-zone fluids, melts and supercritical liquids at 120–180 km depth. Nature 437:724–727

Kessel R, Ulmer P, Pettke T, Schmidt MW, Thompson AB (2005b) The water-basalt system at 4 to 6 GPa: phase relations and second critical endpoint in a K-free eclogite at 700 to 1400 °C. Earth Planet Sci Lett 237:873–892

Klimm K, Blundy JD, Green TH (2008) Trace element partitioning and accessory phase saturation during H_2O-saturated melting of basalt with implications for subduction zone chemical fluxes. J Petrol 49:523–553

Konzett J, Ulmer P (1999) The stability of hydrous potassic phases in lherzolite mantle—an experimental study to 9.5 GPa in simplified and natural bulk compositions. J Petrol 40:629–652

Konzett J, Sweeney RJ, Thompson AB, Ulmer P (1997) Potassium amphibole stability in the upper mantle: an experimental study in a peralkaline KNCMASH system to 8.5 GPa. J Petrol 38:537–568

Kushiro I, Hirose K (1992) Experimental determination of composition of melt formed by equilibrium partial melting of peridotite at high pressures using aggregates of diamond grains. Proc Jpn Acad 68:63–68

Kushiro I, Syono Y, Akimoto S (1968) Melting of a peridotite nodule at high pressures and high water pressures. J Geophys Res 73:6023–6029

Melekhova E, Schmidt MW, Ulmer P, Pettke T (2007) The composition of liquids coexisting with dense hydrous magnesium silicates at 11–13.5 GPa and the endpoint of the solidii in the MgO–SiO_2–H_2O system. Geochim Cosmochim Acta 71:3348–3360

Mengel K, Green DH (1989) Stability of amphibole and phlogopite in metasomatized peridotite under water-saturated and water-undersaturated conditions. In: Kimberlites and related rocks. Geol Soc Aust Spec Publ 14. Ross J (ed) Geological Society of Australia, pp 571–581

Mibe K, Kanzaki M, Kawamoto T, Matsukage KN, Fei Y, Ono S (2007) Second critical endpoint in the peridotite-H_2O system. J Geophys Res 112:B03201

Millhollen GL, Irving AJ, Wyllie PJ (1974) Melting interval of peridotite with 7.5 percent water to 30 kilobars. J Geol 82:575–587

Mysen BO, Boettcher AL (1975) Melting of a hydrous mantle: I. Phase relations of natural peridotite at high pressures and temperatures with controlled activities of water, carbon dioxide, and hydrogen. J Petrol 16:520–548

Nixon PH (ed) (1987) Mantle xenoliths. Wiley, New York

Pawley AR, Wood BJ (1995) The high-pressure stability of talc and 10Å phase: potential storage sites for H_2O in subduction zones. Am Mineral 80:998–1003

Pettke T, Oberli F, Audetat A, Guillong M, Simon AC, Hanley JJ, Klemm LM (2012) Recent developments in element concentration and isotope ratio analysis of individual fluid inclusions by laser ablation single and multiple collector ICP-MS. Ore Geol Rev 44:10–38

Rampone E, Morten L (2001) Records of crustal metasomatism in the garnet peridotites of the Ultwn Zone (Upper Austroalpine, Eastern Alps). J Petrol 42:207–219

Roeder PL, Emslie RF (1970) Olivine–liquid equilibrium. Contrib Mineral Petrol 29:275–289

Schmidt MW, Ulmer P (2004) A rocking multianvil: elimination of chemical segregation in fluid-saturated high-pressure experiments. Geochim Cosmochim Acta 68:1889–1899

Schmidt MW, Vielzeuf D, Auzanneau E (2004) Melting and dissolution of subducting crust at high pressures: the key role of white mica. Earth Planet Sci Lett 228:65–84

Spandler CJ, Pettke T, Hermann J (2014) Experimental study of trace element release during ultrahigh-pressure serpentinite dehydration. Earth Planet Sci Lett 391:296–306

Stalder R (2012) Comment on "The beginnings of hydrous mantle wedge melting" CB Till, TL Grove, Withers, AC, Contrib Mineral Petrol 164:1064–1071. doi:10.1007/s00410-011-0692-6

Stalder R, Ulmer P, Thompson AB, Günther D (2000) Experimental approach to constrain second critical end points in fluid/silicate systems: near-solidus fluids and melts in the system albaite-H_2O. Am Mineral 85:68–77

Stalder R, Ulmer P, Thompson AB, Günther D (2001) High pressure fluids in the system MgO–SiO_2–H_2O under upper mantle conditions. Contrib Mineral Petrol 140:607–618

Stalder R, Ulmer P, Günther D (2002) Fluids in the system forsterite-phlogopite-H_2O at 60 kbar. Schweiz Mineral Petrogr Mitt 82:15–24

Thibault Y, Edgar AD (1992) Experimental investigation of melts from a carbonated phlogopite lherzolite: implications for metasomatism in the continental lithosphere mantle. Am Mineral 77:784–794

Till CB, Grove TL, Withers AC (2012a) The beginning of hydrous mantle wedge melting. Contrib Mineral Petrol 163:669–688

Till CB, Grove TL, Withers AC (2012b) Reply to 'Comment of "The beginnings of hydrous mantle wedge melting" by Till et al.' by Green, Rosenthal and Kovacs. Contrib Mineral Petrol 164:1083–1085

Till CB, Grove TL, Withers AC (2012c) Reply to 'Comment on "The beginnings of hydrous mantle melting" by Till et al.' by Stalder. Contrib Mineral Petrol 164:1073–1076

Toplis MJ (2005) The thermodynamics of iron and magnesium partitioning between olivine an liquid: criteria for assessing and predicting equilibrium in natural and experimental system. Contrib Mineral Petrol 149:22–39

Tumiati S, Fumagalli P, Tiraboschi C, Poli S (2013) An experimental study on COH-bearing peridotite up to 3.2 GPa and implications for crust-mantle recycling. J Petrol 54:453–479

Ulmer P (1989) The dependence of the Fe^{2+}–Mg cation partitioning between olivine and basaltic liquid on pressure, temperature and composition. Contrib Mineral Petrol 101:261–273

Ulmer P (2001) Partial melting in the mantle wedge—the role of H_2O in the genesis of mantle-derived' are-related- magmas. Phys Earth Planet Inter 127:215–232

Wallace ME, Green DH (1991) The effect of bulk rock composition on the stability of amphibole in the upper mantle: implications for solidus positions and mantle metasomatism. Mineral Petrol 44:1–19